Hydrogen Bond Triggers the Self-Assembly of Dihydrogen Arsenates into Supramolecular Anion···Anion Adducts

Cristina Lo Iacono [1], Edem Chakalov [1], Roberta Beccaria, Araghni Bhattacharya, Andrea Pizzi, Peter Tolstoy [*], Giuseppe Resnati [*]

Posted Date: 29 January 2026

doi: 10.20944/preprints202601.2284.v1

Keywords: proton conduction; anion self-assembly

Article

Hydrogen Bond Triggers the Self-Assembly of Dihydrogen Arsenates into Supramolecular Anion···Anion Adducts

Cristina Lo Iacono, [1†] Edem Chakalov, [2†] Roberta Beccaria, [1] Araghni Bhattacharya, [1] Andrea Pizzi, [1] Peter Tolstoy *[2] and Giuseppe Resnati *[1]

[1] NFMLab, Dept. Chemistry, Materials, and Chemical Engineering "Giulio Natta", Politecnico di Milano, Via E. Bassini 6, I-20131 Milano, Italy

[2] Institute of Chemistry, St. Petersburg State University, 26 Universitetskii prospect, Petergof, St. Petersburg 198504, Russia

* Correspondence: peter.tolstoy@spbu.ru (P.T.); giuseppe.resnati@polimi.it (G.R.)

† These authors equally contributed to this work

Abstract

Eight H-bonded complexes of arsenic acid with nitrogen bases (diethylamine, 4-methoxypyridine, pyridine-2,6-diamine, 2,4,6-trimethylpyridine, N^1,N^1,N^2,N^2-tetraethylethane-1,2-diamine, 1,3,5-triazine-2,4,6-triamine, pyridin-4-ol and 4-methoxyaniline) were studied in the solid state by single crystal X-ray diffraction technique and DFT calculations. In all cases quite short (≤ 2.65 Å) OHO bonds were found in the self-assembled supramolecular infinite chains or ribbons of dihydrogen arsenates, constituting a repertoire of five different H-bonding patterns (motifs). The electron localization function maps revealed the spots of the nucleophilic sites on oxygen atoms that determine the preferable directions for H-bonding of $H_2AsO_4^-$ anions observed in the crystal packing. Analysis of the electrostatic potential maps for isolated species has demonstrated that upon H-bonding between $H_2AsO_4^-$ anions and protonated nitrogen bases, $NH^+\cdots{}^-OAsO(OH)_2$, the redistribution of electron density within the anion provides otherwise virtually non-existent electrophilic sites on hydrogen atoms, which balances the Coulomb repulsion and allows for the anion···anion pairing within the crystal. The topological analysis of calculated electron density after relaxation of the hydrogen atoms' positions was used to classify the OHO bonds as moderately strong ones (with an interaction energy up to 65 kJ/mol) and revealed a high degree of ionicity of molecular moieties within zwitterions (with an absolute charge up to 0.87 *e*). For the strongest OHO and NHO bonds the noticeable covalent character was shown by using the crystal orbital Hamiltonian population analysis.

Keywords: proton conduction; anion self-assembly

1. Introduction

In recent years, inorganic acidic anions and organic–inorganic hybrids have attracted increasing attention for their role in functional materials, particularly for applications related to proton conductivity and, in the presence of non-centrosymmetric crystal structures, nonlinear optical properties [1]. In this context, it is now well recognized that efficient proton conduction requires well-organized hydrogen-bond networks capable of facilitating proton transfer via delocalization and hopping mechanisms along supramolecular chains [2–7]. A particularly interesting aspect of these systems is the hydrogen-bond-mediated anion···anion self-assembly, an apparently counterintuitive phenomenon as it involves overcoming the Coulombic repulsion between negatively charged species. This behavior has been rationalized in terms of anti-electrostatic hydrogen bonds (AEHB), which enable the formation of dimers, infinite chains, or extended anionic networks. Depending on

 doi:10.20944/preprints202601.2284.v1

the dimensionality of these supramolecular architectures, hydrogen-bond networks can be classified as 0D (dimers or trimers), 1D, or 2D, according to the extent of the anionic assembly [8,9]. Hydrogen-bond-driven anion···anion self-assembly is well documented for systems containing anions such as HSO_4^-, $H_2PO_4^-$, and HCO_3^- [10–12]. More recent studies have also shown that alternative interactions, such as σ-hole interactions, can contribute to the formation of anion···anion supramolecular adducts, occasionally giving rise to hybrid motifs in which multiple types of interactions cooperate in stabilizing the crystal structure [13]. Structural data reported in the Cambridge Structural Database indicate that such phenomena are not rare and can lead to infinite supramolecular chains or anionic dimers stabilized by hydrogen-bond networks [14,15]. In this context, dihydrogen arsenate anions ($H_2AsO_4^-$) represent a system of great interest but remain relatively less explored compared to their sulfate and selenate analogues. Several literature examples show that $H_2AsO_4^-$ anions can self-assemble into extended supramolecular structures through AsO–H···OAs hydrogen bonds in the presence of nitrogen-containing organic cations, both aromatic and aliphatic. These architectures, often featuring non-centrosymmetric infinite chains, appear particularly promising as candidates for high proton-conductivity materials [16–21]. Moreover, extended hydrogen-bond networks based on arsenate anion···anion assembly have also been linked to proton delocalization phenomena relevant for photonic applications [22,23]. Proton conductivity in these materials is strongly influenced by several factors, including hydrogen-bond strength, cooperative coupling between adjacent bonds, and the degree of proton delocalization within O–H···O bonds [24]. A thorough understanding of these aspects is essential for the rational design and functional optimization of materials based on $H_2AsO_4^-$···$H_2AsO_4^-$ supramolecular synthons. In this work, we present a systematic study of hydrogen-bond-mediated anion···anion motifs in the supramolecular assemblies of dihydrogen arsenates. Eight salts obtained from arsenic acid with various nitrogen bases (Scheme 1) were investigated in the solid state using single-crystal X-ray diffraction and density functional theory (DFT) calculations. Structural analysis revealed the presence of particularly short O–H···O bonds, organized into infinite chains or supramolecular ribbons, defining distinct hydrogen-bond motifs. The integration of crystallographic data with theoretical analyses of electron density, electrostatic potential, and bonding interactions allows elucidation of the electronic and structural factors underlying anion···anion self-assembly in dihydrogen arsenates, as well as the key role of proton delocalization in stabilizing these architectures.

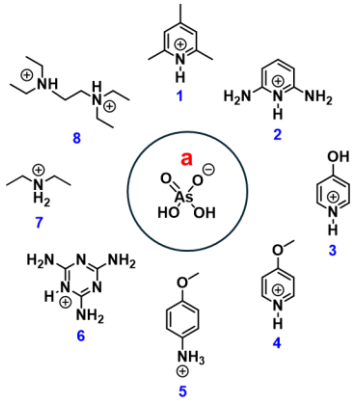

Scheme 1. Structural formulas of the components in the crystal structures described in this work.

2. Materials and Methods

2.1. Materials

All compounds were purchased from commercial suppliers (Sigma-Aldrich, TCI America, and Merck) and used without further purification. The arsenic acid (H_3AsO_4) solution was prepared by dissolving 1.150 g of arsenic pentoxide (As_2O_5) in 100 mL of distilled water, followed by reflux at 100 °C for 5 weeks [25]. The concentration of the resulting acid solution was determined by titration with

 doi:10.20944/preprints202601.2284.v1

NaOH using a pH meter and found to be 0.1 M, consistent with the quantitative hydrolysis of As_2O_5 to H_3AsO_4.

Crystal sample preparation: All salts were prepared according to the following procedure. Separate aqueous solutions (0.1 mmol) containing equimolar amounts of arsenic acid and the corresponding monoprotic base were mixed under constant stirring. The solutions were then left to slowly evaporate at room temperature in clear 4 mL borosilicate vials. Single crystals suitable for X-ray diffraction were obtained within two weeks.

2.2. Methods

2.2.1. Characterization

X-ray diffraction analysis: Data collections were performed at 300K or 100 K using an XtaLAB Synergy diffractometer equipped with a HyPix detector. Unit cell refinement and data reduction were performed using CrysAlisPro (version 1.171.41.98a) software [26]. Structures were solved by direct methods using SHELXT [27] program and refined by full-matrix least-squares on F^2 with anisotropic displacement parameters for the non-hydrogen atoms using the SHELXL [28] program incorporated in the Olex2 (version 1.5) software [29]; hydrogen atoms were placed in idealized positions and firstly refined using a riding model, and subsequently additionally refined as described in the next subsection. Absorption correction was performed based on the multiscan procedure. X-ray structures were visualized using capped sticks representation built in the Mercury (version 2022.3.0) software [30]. CCDC deposition numbers: 2521265, 2521276, 2521277, 2521278, 2521279, 2521280, 2521281, 2521284 contain the validated [31] supplementary crystallographic data for this paper (see ESI). These data are provided free of charge by the joint Cambridge Crystallographic Data Centre and Fachinformationszentrum Karlsruhe Access Structures service.

Solid-state calculations. Electronic calculations of **1a**-**8a** were performed using the CRYSTAL17 (version 1.0.2)[32] software. Constrained geometry optimizations were done at the B3LYP-D*/POB-TZVP [33–38] level of theory. The chosen combination of the DFT functional and the atomic basis set has been shown to reproduce the H-bond geometric features of the supramolecular chains of hydrogen selenates ($HSeO_4^-$) with sufficient accuracy, see our recent work [14]. Accuracy of calculation of the Coulomb and Hartree–Fock exchange series was controlled by a set of overlap tolerances, which were taken to be (10^{-9}, 10^{-9}, 10^{-9}, 10^{-9}, 10^{-18}).[39] The maximum order of multipole expansion [41,42] in the long-range zone for the electron-electron Coulomb interaction was set to 6. Calculation of the DFT exchange-correlation contribution over the unit cell volume was done with the *XLGRID* DFT grid specification; [39–42] tolerances for the DFT density and the DFT grid weight were taken to be 10^{-10} and 10^{-18}, respectively. Integration in the Brillouin zone was performed using the Monkhorst–Pack scheme [43] for an anisotropic 8×4×4 (for **6a**), 6×8×3 (for **4a**), 4×8×2 (for **3a**), 8×6×6 (for **2a** and **8a**), 4×6×6 (for **5a**) and 8×5×8 (for **7a**) ***k***-point grids, and for an isotropic 6×6×6 ***k***-point grid for **1a**. DIIS [44] tolerance on energy controlling the SCF convergence for geometry optimizations and single-point calculations was set to 10^{-8} and 10^{-9} Hartree, respectively.

Single-crystal structure parameters of the above crystals from the X-ray diffraction data at 300 and 100 K were used as the starting points for the DFT calculations. While keeping fixed the unit cell parameters and heavy atoms' positions, all hydrogen atoms' positions were optimized with tight convergence criteria (maximum/RMS forces and displacements smaller than 0.000075/0.000050 a.u. and 0.000225/0.000150 a.u., respectively) and symmetry constraint imposed by the corresponding space group: triclinic $P\bar{1}$ for **2a**, **6a**, and **8a**; monoclinic $P2_1/n$ for **4a** and **7a**, $P2_1/m$ for **1a**, and $P2_1/c$ for **3a** and **5a**. For **1a** featuring dynamically disordered hydrogen atoms of methyl groups of the protonated 2,4,6-trimethylpyridine molecules, the structures of eight different ordered isomorphs were subjected to the above constrained geometry optimization; afterwards, only one of the optimized structures (see Figs. S27 and S28) was selected for further calculations which are described onwards. Analytical energy gradients [45] within a quasi-Newton approach combined with the BFGS [46] algorithm for Hessian updating were used. Consistency between the optimized geometries and

 doi:10.20944/preprints202601.2284.v1

the aforementioned overlap tolerances for integrals' evaluation was ensured by the *FINALRUN* option with the value of 4 [39].

Topological analysis [47,48] of the periodic electron density (ED) was performed using quantum theory of atoms in molecules (QTAIM) by means of the TOPOND14 module [49] implemented in the CRYSTAL17 code [50]. AIM atomic charges were evaluated by integration of the three-dimensional density distribution over the atomic basins, whose enclosing zero-flux surfaces were determined manually to the nearest preliminary retrieved bond critical point for a given nucleus using an eigenvector following approach with the tolerance value of 0.002 a.u.[51–53].

Crystal orbital Hamiltonian population projected onto local atomic orbitals pertaining to two selected groups of H and A (A = O or N) atoms, involved in the H···A hydrogen-bonding, was calculated over the energy range spanned from the first valence band, occupied by the non-core electrons, up to the highest occupied valence band, *i.e.* up to the Fermi energy level. The Hamiltonian eigenvectors were preliminary recalculated using a fine isotropic 12×12×12 ***k***-point grid.

Molecular calculations. Electronic calculations of the molecular adducts analyzed in this work were performed using the Gaussian16 (version A.01) software [54]. Single-point calculations with standard tolerance on energy controlling the SCF convergence were performed at the PW6B95-D3(BJ)/def2-TZVPD level of theory [55–58]. The basis set superposition error for the calculation of complexation (or interaction) energies was corrected using the counterpoise method [59]. The ED, molecular ESP [60], and electron localization function (ELF [61]) surfaces were calculated using the MultiWFN (version 3.8) software [62,63]. The ELF isosurfaces were mapped at 0.87 isovalue.

Manipulation and visualization of the crystal and molecular structures was done using the BIOVIA's Materials Studio [64] and GaussView software [65], respectively. Graphs were plotted using the Origin software [66].

3. Results and Discussion

In this work, eight crystal structures are reported, all containing a single unique zwitterion consisting of the $H_2AsO_4^-$ anion hydrogen-bonded to the corresponding protonated nitrogen base within the primitive unit cell. The crystals belong to triclinic (**2a**, **6a**, **8a**) or monoclinic (**1a**, **3a**, **4a**, **5a, 7a**) lattices. The presence of only one independent zwitterion in the unit cell accounts for the observation of only two—or, in some cases, only one—distinct O–H···O hydrogen bonds between the anions, depending on the relative positions of the cations. From a structural viewpoint, compounds **1a**, **2a**, **4a**, **7a**, and **8a** adopt anion···anion assemblies in the form of infinite linear chains, whereas **3a** and **6a** exhibit ribbon-like anion assemblies. Compound **5a** represents a unique case, displaying an anion···anion self-assembly organized into a two-dimensional (2D) network.

2,4,6-Trimethylpyridinium dihydrogen arsenate (**1a**), crystallizes in the $P2_1/m$ space group. In this compound, the average O···O distance within the AsO–H···O hydrogen bond is 2.622 Å, a remarkably short value indicative of a strong hydrogen bond, which enables the $H_2AsO_4^-$ anions to self-assemble while overcoming electrostatic anion–anion repulsion. Shorter O···O distances are observed in compounds **2a** (already known in another polymorphic form [67]), **4a**, **7a**, and **8a**, as summarized in Table 1. This consistent trend toward short O···O separations suggests the presence of a robust network of $H_2AsO_4^-$ anions stabilized by so-called "anti-electrostatic" hydrogen bonding.

Table 1. Space group and the list of the O···O distances.

Salt	Space group	O···O distances
1a	P $2_1/m$	2.622 Å
2a	P$\bar{1}$	2.632 Å 2.600 Å
3a	P $2_1/c$	2.575 Å 2.602 Å
4a	P $2_1/n$	2.603 Å 2.608 Å

 doi:10.20944/preprints202601.2284.v1

5a	P $2_1/c$	2.587 Å 2.605 Å
6a	$P\bar{1}$	2.593 Å 2.554 Å
7a	$P\bar{1}$	2.585 Å 2.609 Å
8a	P $2_1/n$	2.604 Å 2.634 Å

The crystal structures are stabilized by electrostatic attraction between oppositely charged cations and anions, as well as by a variety of non-covalent interactions spanning a wide range of lengths and strengths. These include: (i) major O–H···O and N–H···O hydrogen bonds (ii) π-stacking interactions between N-heterocycles, observed in compounds **1a**-**6a**; and (iii) numerous additional minor C–H···O contacts. Among the studied crystals, **1a**, **2a**, and **4a** clearly show that aromatic cations engage in π–π stacking interactions, leading to the formation of spatially segregated cationic and anionic regions. This arrangement facilitates anion···anion pairing through hydrogen bonding, as directly observed in their crystal structures. In contrast, crystals containing 4-hydroxypyridinium (**3a**) melaminium (**6a**) and 4-methoxy anilinium (**5a**) cations display ribbon-like anion···anion assemblies. In these cases, $H_2AsO_4^-$ dimers propagate along the crystallographic *b* axis, with O···O distances ranging from 2.554 to 2.602 Å. Close contacts between anions and cations, characterized by N···O distances of 2.61–2.78 Å, contribute to the redistribution of negative charge within the anion, thereby enabling the formation of short inter-anionic O–H···O hydrogen bonds (2.56–2.64 Å). All major hydrogen bonds involving $H_2AsO_4^-$ anions are fairly linear, with angles in the ranges 169° < ∠(OHO) < 179° and 131° < ∠(NHO) < 179° in computationally optimized structures. The crystal packings of the studied compounds are shown in Figures S1–S8 in the Electronic Supporting Information (ESI). The association motifs of the amphoteric dihydrogen arsenate anions, which can simultaneously act as hydrogen-bond donors and acceptors, are more readily discussed in conjunction with the results of density functional theory (DFT) calculations performed on the same crystals. Acknowledging the intrinsic difficulty of X-ray diffraction techniques in accurately locating hydrogen atoms, the hydrogen positions were selectively relaxed while keeping the remaining unit-cell parameters fixed (see Table S1 and the resulting structures in Figures 1–4). Analysis of these optimized structures allows five distinct motifs of "anti-electrostatic" [68] hydrogen bonding to be identified: tightly linked chains of cyclic dimers (motifs 1 and 2 in Figures 1 and 2), loosely linked chains and slabs of cyclic dimers (motifs 3 and 5 in Figures 3 and 4), and a tightly linked chain of cyclic trimers (motif 4 in Figure 3). The non-equivalent O–H···O hydrogen bonds between anions are highlighted in different colors in Figures 1–4. The spatial arrangement of the hydrogen-bond networks in the studied crystals is further constrained by the anisotropy of the outer electronic shell of the proton-accepting oxygen atoms, which dictates the preferred directions for the formation of O–H···O and N–H···O bonds involving the $H_2AsO_4^-$ anions. This anisotropy originates from lone-pair domains, which give rise to toroidal and bean-shaped isosurfaces of the electron localization function (ELF) in the As–$O^{\delta-}$ and As–O–H groups, respectively (see Figures S9–S16). The ELF isosurfaces are very similar for the isolated anion and for the corresponding zwitterion considered in the X-ray-derived geometry.

Preprints.org (www.preprints.org) | NOT PEER-REVIEWED | Posted: 29 January 2026 doi:10.20944/preprints202601.2284.v1

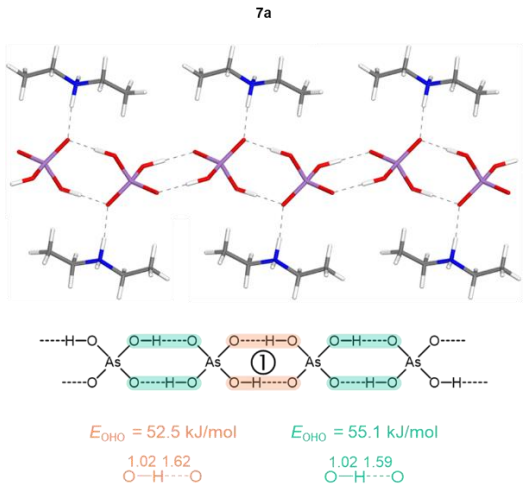

Figure 1. Partial view of the H-bonded chains in **7a** with optimized positions of the hydrogen atoms (motif 1 of $H_2AsO_4^-$ anions' assembling). Interatomic distances are given in Å. Bond energies, E_{OHO}, are estimated from the electronic kinetic energy density values at BCP, G_{bcp} (see Table 2).

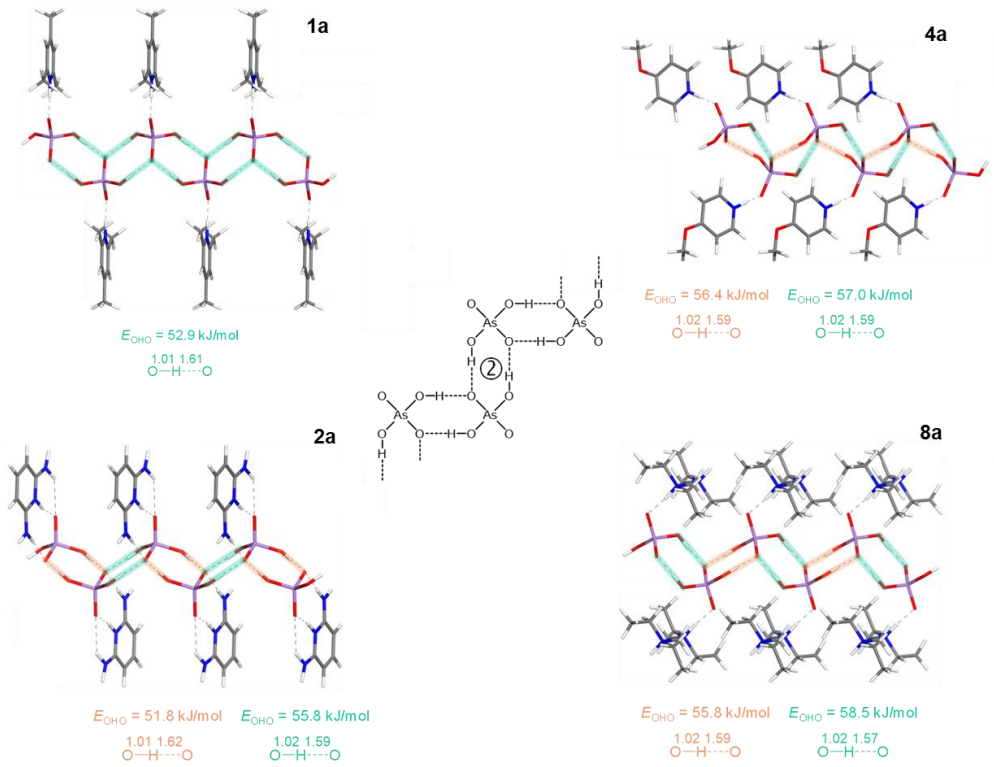

Figure 2. Partial view of the H-bonded chains in **1a, 2a, 4a** and **8a** with optimized positions of the hydrogen atoms (motif 2 of $H_2AsO_4^-$ anions' assembling). Interatomic distances are given in Å. E_{OHO} values are estimated from the G_{bcp} values (see Table 2).

 doi:10.20944/preprints202601.2284.v1

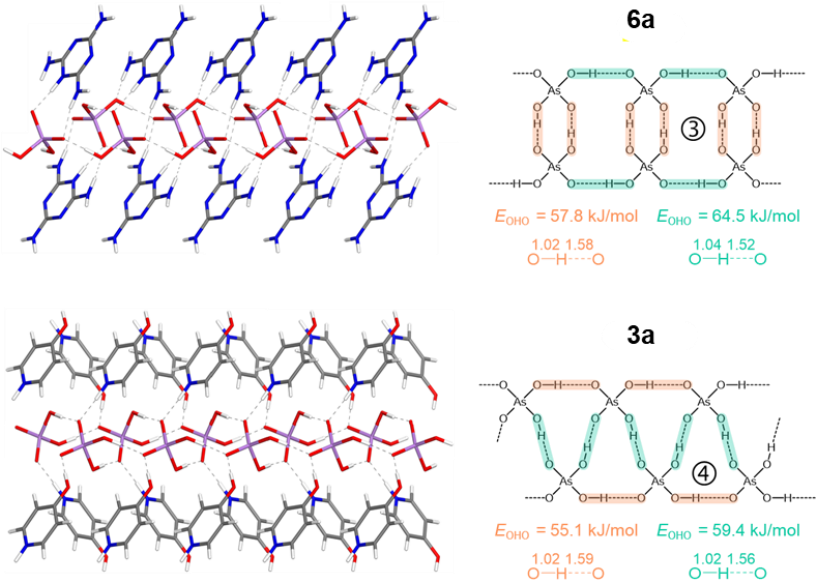

Figure 3. Partial view of the H-bonded chains in **6a** and **3a** with optimized positions of the hydrogen atoms (motifs 3 and 4 of $H_2AsO_4^-$ anions' assembling, respectively). Interatomic distances are given in Å. E_{OHO} values are estimated from the G_{bcp} values (see Table 2).

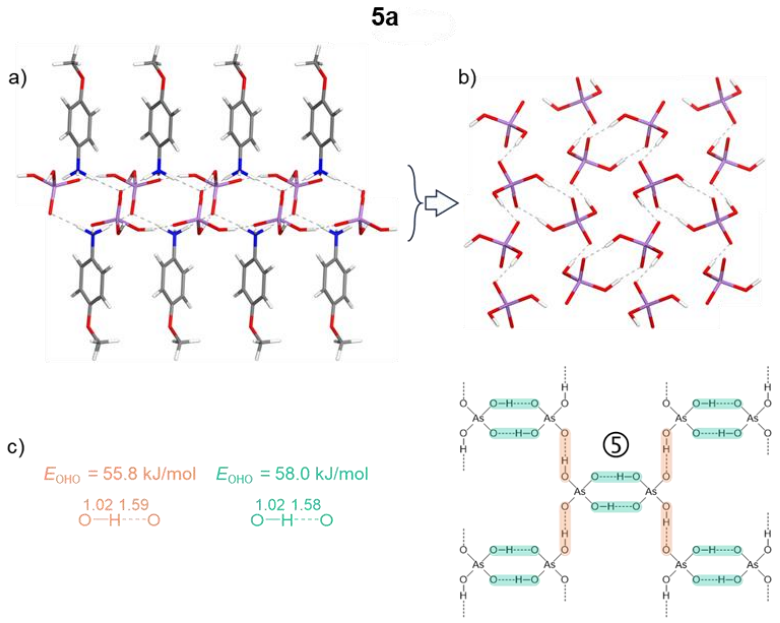

Figure 4. Partial view of the chainmail-like H-bonded slabs in **5a** with optimized positions of the hydrogen atoms (motif 5 of $H_2AsO_4^-$ anions' assembling). (a): side view, (b): top view. Interatomic distances are given in Å. E_{OHO} values (c) are estimated from the G_{bcp} values (see Table 2).

The 3D ESP maps represented *via* ED isosurfaces color-coded with the ESP values are shown in Fig. 5 for isolated $H_2AsO_4^-$ anions and their complexes with counter cations in crystalline geometry. Note that the color-coded ranges of ESP values are not symmetric and different in each case, being selected for maximum contrast between various regions. The key difference between isolated anions and zwitterions is in the electrophilicity of $H_2AsO_4^-$ fragment. The entire surface is negative for the isolated anions, but polarization effects in the zwitterions creates electrophilic sites on the hydrogen atoms of the As–O–H groups: the negative extremum of ESP around H atoms changes to the positive one (see the values given in Fig. 5). Thus, the ESP maps demonstrate that redistribution of the negative charge of $H_2AsO_4^-$ anion by adjacent cation is crucial to drive the self-assembly of the anions in all studied crystals. Indeed, the complexation between isolated $H_2AsO_4^-$ anions in crystalline

 doi:10.20944/preprints202601.2284.v1

geometry is energetically unfavorable: significant electrostatic repulsion hampers self-association, as evidenced by additional calculations results of which are shown in Fig. S17.

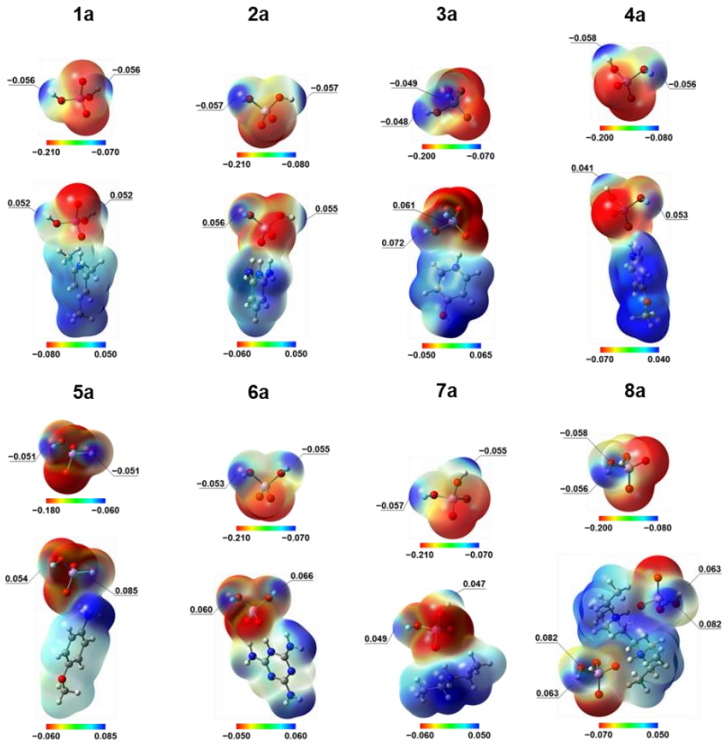

Figure 5. ED 0.001 a.u. isosurfaces mapped by the molecular electrostatic potential (MESP) for $H_2AsO_4^-$ anion and the corresponding zwitterion in the X-ray geometries of the studied crystals (calculated at PW6B95-D3(BJ)/def2-TZVPD level of theory) but with preoptimized positions of the hydrogen atoms (at B3LYP-D*/POB-TZVP level of theory). Different color scales are used for the MESP (in a.u.).

Within the QTAIM methodology, the nature of an H-bond can be described by the topological properties of the electron density (ED), ρ, and various functions derived from it at the bond critical point (BCP) between the bridging proton and the proton-accepting atom.[69–77] For example, the signs of $\nabla^2\rho_{bcp}$ (*i.e.* the Laplacian of the ED) and $H_{bcp} = G_{bcp} + V_{bcp}$ (*i.e.* the total electronic energy density as a sum of the kinetic and potential energy densities G_{bcp} and V_{bcp} at the BCP) are used to differentiate between three types of interactions: non-covalent (region I, $\nabla^2\rho_{bcp} > 0$, $H_{bcp} > 0$), covalent (region II, $\nabla^2\rho_{bcp} < 0$, $H_{bcp} < 0$), and partially covalent (region III, $\nabla^2\rho_{bcp} > 0$, $H_{bcp} < 0$). Since $V < 0$ and $G > 0$, the sign of H_{bcp} reveals whether V_{bcp} or G_{bcp} dominate in the bonding region: a dominance of V_{bcp} ($H_{bcp} < 0$) indicates that accumulation of electronic charge in the internuclear region is stabilizing; conversely, if $G_{bcp} > V_{bcp}$, ($H_{bcp} > 0$), the internuclear charge accumulation is destabilizing, which is typical for a non-covalent interaction. The boundaries between regions I, II, and III are defined by $H_{bcp} = 0$ (*i.e.* $|V_{bcp}|/G_{bcp} = 1$) and by $\nabla^2\rho_{bcp} = 0$ (*i.e.* $|V_{bcp}|/G_{bcp} = 2$ from the virial equation). Within region I, the higher is the bond degree index (BDI) H_{bcp}/ρ_{bcp}, the weaker the interaction. Similarly, in regions II and III, the higher is the BDI, the higher the covalent character of the interaction.

For all studied structures, the calculated values of the above outlined parameters at the intermolecular BCPs of the OHO bonds between $H_2AsO_4^-$ anions are listed in Table 2. These bonds, being similar to each other, exhibit quite large ρ_{bcp} values of approximately 0.06 a.u. but positive $\nabla^2\rho_{bcp}$ values indicating a locally charge depleted domain, which places these bonds in region III at the border with region I, characterizing them as non-covalent interactions with a small degree of covalency.[78] This finding is in agreement with the relative values of other H-bond descriptors, meeting the inequalities $1 < |V_{bcp}|/G_{bcp} < 2$, $G_{bcp}/\rho_{bcp} < 1$ (the kinetic energy per electron, in a.u.), and $H_{bcp}/\rho_{bcp} < 0$. The hydrogen bond energies, E_{OHO}, estimated using the equation $E_{OHO} = 0.429\ G_{bcp}$,[79,80]

 doi:10.20944/preprints202601.2284.v1

fall in the range 51 < E_{OHO} < 65 kJ/mol with an average value of 56 kJ/mol. Noteworthy, the full set of QTAIM parameters, the estimated H-bond energies, and the O...O interatomic distances for the interacting $H_2AsO_4^-$ anions are similar to those for the recently studied interacting $HSeO_4^-$ anions [24], for which we have predicted the thermally accessible vibrational motion of the bridging protons from one heavy atom to another in double-well potentials. For completeness, in ESI we provide QTAIM parameters at the intermolecular BCPs of the NHO bonds between cations and anions (as well as analogous OHO bond in case of **3a**), and also NHN bonds between cations in **6a**, see Figs. S18–S25 and Table S2. In a nutshell, the ρ, $\nabla^2\rho$, V, G, $|V|/G$, H and H/ρ values indicate that appertaining H-bonds in studied crystals can be classified as follows: (i) OHO, moderately strong bond (72 kJ/mol); (ii) NHO, from weak to moderately strong bonds (9 < E_{NHO} < 66 kJ/mol); (iii) NHN, weak bonds (21 < E_{NHN} < 24 kJ/mol). Despite the short N...O distances between cations and anions, the strong proton displacements towards nitrogen atoms (almost complete proton transfers) lead to a large degree of charge separation: the absolute values of AIM charges of the interacting molecular moieties are 0.81–0.87 *e* (see Table S3). Furthermore, an AIM charge of the bridging hydrogen atom might be considered as an additional descriptor of the H-bond strength that performs well over a sufficiently wide sampling, which is shown for NHO bonds in Fig. S26a.

Table 2. QTAIM parameters (in a.u.) at the intermolecular BCPs of the OHO bonds between $H_2AsO_4^-$ anions, and estimated corresponding bond energies (in kJ/mol), E_{OHO} = 0.429 G_{bcp} [79,80] for **1a-8a**.

	1a	**2a**	**3a**	**4a**	**5a**	**6a**	**7a**	**8a**
ρ_{bcp}	0.0562	0.0548	0.0582	0.0601	0.0598	0.0617	0.0561	0.0596
		0.0594	0.0638	0.0607	0.0612	0.0719	0.0590	0.0630
$\nabla^2\rho_{bcp}$	0.1311	0.1307	0.1358	0.1347	0.1337	0.1367	0.1299	0.1340
		0.1344	0.1376	0.1355	0.1388	0.1334	0.1330	0.1357
G_{bcp}	0.0469	0.0460	0.0489	0.0500	0.0495	0.0513	0.0466	0.0496
		0.0496	0.0528	0.0506	0.0515	0.0572	0.0489	0.0520
G_{bcp}/ρ_{bcp}	0.8345	0.8394	0.8402	0.8319	0.8278	0.8314	0.8307	0.8322
		0.8350	0.8276	0.8336	0.8415	0.7955	0.8288	0.8254
V_{bcp}	-0.0611	-0.0594	-0.0638	-0.0664	-0.0656	-0.0684	-0.0607	-0.0656
		-0.0655	-0.0711	-0.0673	-0.0683	-0.0812	-0.0646	-0.0700
$\|V_{bcp}\|/G_{bcp}$	1.3016	1.2901	1.3057	1.3270	1.3250	1.3334	1.3028	1.3241
		1.3219	1.3481	1.3304	1.3263	1.4176	1.3204	1.3473
H_{bcp}	-0.0142	-0.0134	-0.0149	-0.0164	-0.0161	-0.0171	-0.0141	-0.0161
		-0.0160	-0.0184	-0.0167	-0.0168	-0.0239	-0.0157	-0.0181
H_{bcp}/ρ_{bcp}	-0.2520	-0.2437	-0.2569	-0.2725	-0.2688	-0.2770	-0.2514	-0.2695
		-0.2686	-0.2880	-0.2752	-0.2747	-0.3324	-0.2659	-0.2867
E_{OHO}	52.87	51.84	55.07	56.37	55.76	57.75	52.48	55.83
		55.83	59.43	56.99	58.03	64.48	55.13	58.53

It is well-known that the electronic density of states (DOS) analysis provides valuable insight into the contribution of particular local atomic orbitals (AOs) to the overall electronic structure of solids over a specified energy range [81–85]. Projected crystal orbital Hamiltonian population (COHP) analysis is an extension of the DOS analysis aimed to characterize pairwise interactions between two atoms (two discrete groups of AOs) in solids [86–89]. By weighing DOS by the Hamiltonian matrix, COHP partitions the band energies into bonding (stabilizing) and antibonding (destabilizing) regions, thus providing information regarding the partial covalent character of hydrogen···acceptor interactions in molecular solids [90,91]. In this context, COHP analysis has

 doi:10.20944/preprints202601.2284.v1

proven itself to be complementary to the QTAIM analysis. Both approaches, being fundamentally different, share the same concept of gauging the nature and strength of H-bonds as a tangible quantity in a solid directly from its underlying electronic structure. An estimate of the covalent contribution to H-bonding interaction can be made by integrating stabilizing (negative) and destabilizing (positive) regions of the projected COHP values up to the highest occupied band, *i.e.* the Fermi energy level (ε_F), giving so-called IpCOHP values. In Fig. 6, –IpCOHP values are plotted against the corresponding H-bond lengths R(AH···O) and ρ_{bcp} densities for pairs of atoms involved in the AH···O interactions (A = O or N) for all studied structures. One obtains a variety of stabilizing interaction energies in the range 0–260 kJ/mol. On the one hand, the larger values in this set correlate reasonably well with R(AH···O) and ρ_{bcp} values, similarly to what was previously observed for short OHO bonds, (see Figs. 2 and 3 in Ref. 90). It is also appreciable that weak NHN bonds in **6a**, although there are only two unique ones of them, follow the same trend (green symbols in Fig. 6). On the other hand, there is a group of −IpCOHP values that tightly cluster around zero (circled data points in Fig. 6) regardless the OH···O (NH···O) interatomic distance or the electronic charge concentration at the BCP. For OHO bonds (red symbols in Fig. 6) this means that stabilizing and destabilizing pCOHP regions effectively cancel each other over the entire valence region, which indicates that the H-bonding anion–anion interactions are essentially closed-shell electrostatic in nature. An exception is the following three OHO bonds with significant covalent contribution: the strongest among motifs 1–5 OHO bonds linking $H_2AsO_4^-$ dimers in **6a** (highlighted in green in Fig. 3), the strongest and unique among studied structures OHO bonds between protonated pyridinium-4-ol cations and $H_2AsO_4^-$ anions (see Fig. S20) in **3a**, and moderately strong OHO bonds in the tightly linked chains of $H_2AsO_4^-$ cyclic trimers in the same structure (highlighted in pale orange in Fig. 3). In other words, it seems that the covalent character of an anion···anion interaction becomes detectable by the –IpCOHP values if either the bond is very strong (short) or the negative charge of the anion is strongly shifted towards the tightly bound cation. In case of **3a** such charge redistribution is facilitated by the fact that both OHO bonds in question (anion···anion and anion···cation ones) share the same acceptor atom. For NHO bonds (blue symbols in Fig. 6), the −IpCOHP values are close to zero for three data points (circled in Fig. 6), which correspond to H-bonds that involve one H atom of the NH_2^+ group in **7a** and two H atoms of the NH_3^+ group in **5a** (see Figs. S24 and S22). Now it is not clear which feature of these interactions leads to such small −IpCOHP values. Comparison of the OH···O, NH···O, and NH···N interaction energies obtained by QTAIM and COHP analyses reveals that an increase of the covalent contribution to the interaction energy upon the bond strengthening is not always fulfilled.

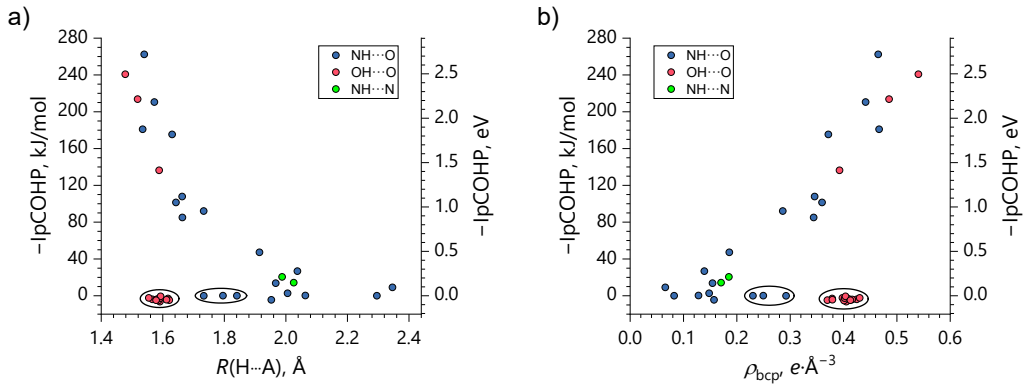

Figure 6. Dependencies of the negative integrated to the ε_F level projected COHP values (−IpCOHP) for the OH···O, NH···O, and NH···N interactions in all studied crystals on the corresponding interatomic R(H···A) distances (A = O, N) (a) and ρ_{bcp} densities (b).

4. Conclusions

Eight crystalline salts of arsenic acid with nitrogen-containing bases were investigated to analyze hydrogen-bond-mediated anion···anion self-assembly in dihydrogen arsenates. Single-

 doi:10.20944/preprints202601.2284.v1

crystal X-ray diffraction shows that, in all structures, $H_2AsO_4^-$ anions are involved in short and nearly linear O–H···O hydrogen bonds (O···O ≤ 2.65 Å), leading to the formation of extended supramolecular architectures. Depending on the crystal packing, these interactions generate infinite chains, ribbon-like assemblies, or a two-dimensional anionic network. On this basis, five recurrent hydrogen-bonding motifs were identified. Density functional theory calculations were used to rationalize the experimental observations. Electron localization function analysis indicates that the anisotropic distribution of lone-pair electron density on oxygen atoms governs the preferred directions of hydrogen bonding. Electrostatic potential maps show that interaction with protonated nitrogen bases induces a redistribution of electron density within the $H_2AsO_4^-$ anion, creating electrophilic regions on the As–O–H hydrogen atoms that enable anion···anion association despite Coulombic repulsion. Topological analysis of the electron density classifies the inter-anionic O–H···O hydrogen bonds as moderately strong interactions, with estimated energies in the range of 50–65 kJ/mol and a limited covalent contribution. The zwitterionic building blocks display a high degree of ionicity, with AIM charges approaching ±0.87 e. Complementary COHP analysis indicates that most anion···anion hydrogen bonds are predominantly electrostatic, while a measurable covalent component is observed only for the shortest O–H···O contacts or in cases of pronounced cation-induced charge redistribution. Overall, this study provides a systematic structural and electronic description of hydrogen-bond-driven anion···anion self-assembly in dihydrogen arsenates. The identified motifs and bonding characteristics contribute to the understanding of anti-electrostatic hydrogen bonding in inorganic acidic anions and may assist in the analysis of related hydrogen-bonded arsenate systems.

Data Availability Statement: The data supporting this article have been included as part of the Supplementary Information. Crystallographic data of compounds described in this paper have been deposited at the CCDC under Deposition Numbers 2521278 (for 1a), 2521277 (for 2a), 2521281 (for 3a), 2521276 (for 4a), 2521284 (for 5a), 2521280 (for 6a), 2521265 (for 7a) and 2521279 (for 8a) can be obtained free of charge from https://www.ccdc.cam.ac.uk/

Conflicts of Interest: There is no conflict of interest.

Appendix B

All appendix sections must be cited in the main text. In the appendices, Figures, Tables, etc. should be labeled starting with "A"—e.g., Figure A1, Figure A2, etc.

References

1. Stejskal, J.; Havlíček, D.; Císařová, I.; Matulková, I. Vibrational Spectroscopic and X-Ray Single Crystal Diffraction Investigation of Tetra-n-Alkylammonium Hydrogen Selenates. *J. Chem. Crystallogr.* **2017**, *47*, 59–68. doi: 10.1007/s10870-017-0680-4.
2. Belushkin, A. V.; Carlile C. J.; Shuvalov, L. A. A quasielastic neutron scattering study of protonic transport in hydrogen-bonded alkali metal hydrogen sulphates and selenates. *Ferroelectrics* **1995**, *167*, 21–31. doi: 10.1080/ 00150199508007716.
3. Ikeda, S.; Yamada, Y. Phase transition in hydrogen bonded ferroelectric compounds—Quantum fluctuations versus thermal fluctuations. *Phys. B Condens. Matter* **1995**, *213–214*, 652–657. doi: 10.1016/0921-4526(95)00240-A.
4. Pavlenko, N. I. Protonic conductivity at the superionic phase transitions in the $M_3H(XO_4)_2$ crystal group. *J. Phys.: Condens. Matter* **1999**, *11*, 5099–5110. doi: 10.1088/0953-8984/11/26/311.
5. Pavlenko, N.; Pietraszko, A.; Pawlowski, A.; Polomska, M.; Stasyuk I. V.; Hilczer, B. Hydrogen transport in superionic system $Rb_3H(SeO_4)_2$: a revised cooperative migration mechanism. *Phys. Rev. B: Condens. Matter Mater. Phys.* **2011**, *84*, 1–10. doi: 10.1103/PhysRevB.84.064303.
6. Matsui, H.; Shimatani, K.; Ikemoto, Y.; Sasaki T.; Matsuo, Y. Phonon-assisted proton tunneling in the hydrogen-bonded dimeric selenates of $Cs_3H(SeO_4)_2$. *J. Chem. Phys.* **2020**, *152*, 154502. doi: 10.1063/1.5145108.

 doi:10.20944/preprints202601.2284.v1

7. Matsui, H.; Fukuda, K.; Takano, S.; Ikemoto, Y.; Sasaki T.; Matsuo, Y. Mechanisms of the antiferro-electric ordering in superprotonic conductors $Cs_3H(SeO_4)_2$ and $Cs_3D(SeO_4)_2$. *J. Chem. Phys.* **2022**, *156*, 204504. doi: 10.1063/5.0088230.
8. Rajbanshi, A.; Wan, S.; Custelcean, R. Dihydrogen Phosphate Clusters: Trapping $H_2PO_4^-$ Tetramers and Hexamers in Urea-Functionalized Molecular Crystals. *Cryst Growth Des* **2013**, *13*, 2233–2237. doi:10.1021/cg400336q.
9. Zhao, W.; Flood, A.H.; White, N.G. Recognition and Applications of Anion–Anion Dimers Based on Anti-Electrostatic Hydrogen Bonds (AEHBs). *Chem Soc Rev* **2020**, *49*, 7893–7906. doi:10.1039/D0CS00486C.
10. Pizzi, A.; Dhaka, A.; Beccaria, R.; Resnati, G. Anion···anion self-assembly under the control of σ- and π-hole bonds. *Chem. Soc. Rev.* **2024**, *53*, 6654. doi: 10.1039/D3CS00479A.
11. Beccaria, R.; Dhaka, A.; Calabrese, M.; Pizzi, A.; Frontera, A.; Resnati, G. Chalcogen and Hydrogen Bond Team up in Driving Anion···Anion Self-Assembly. *Chem. Eur. J.* **2024**, *30*, e202303641. doi: 10.1002/chem.202303641.
12. Drozd M.; Baran, J. Polarized IR-microscope spectra of guanidinium hydrogenselenate single crystal. *Spectrochim. Acta Part A* **2005**, *61*, 2953–2965. doi: 10.1016/j.saa.2004.11.007.
13. Lorenc, J.; Bryndal, I.; Marchewka, M.; Kucharska, E.; Lis. T.; Hanuza, J. Crystal and molecular structure of 2-amino-5-chloropyridinium hydrogen selenate—its IR and Raman spectra, DFT calculations and physicochemical properties. *J. Raman Spectrosc.* **2008**, *39*, 863–872. doi: 10.1002/jrs.1925.
14. Akriche S.; Rzaigui, M. 2-Amino-3-nitropyridinium hydrogen selenate. *Acta Crystallogr., Sect. E.* **2009**, *65*, o1648. doi: 10.1107/ S1600536809022879.
15. Maalej, W.; Ben Rached, A.; Mhiri, T.; Daoud, A.; Zouari, N.; Elaoud, Z. Vibrational study, phase transitions and electrical properties of 4-benzylpyridinium monohydrogenselenate. *J. Phys. Chem. Solids* **2016**, *96–97*, 92–99. doi: 10.1016/j.jpcs.2016.05.010.
16. Janczak, J.; Perpétuo, G. J. Hydrogen-Bonded Networks in Crystals of 1-(Diaminomethylene)Thiouron-1-Ium Perchlorate, Hydrogen Sulfate, Dihydrogen Phosphate and Dihydrogen Arsenate. *Acta Crystallogr., Sect. C* **2008**, *64*, o330–o334. doi:10.1107/S0108270108013504.
17. Chtioui, A.; Benhamada, L.; Jouini, A. Crystal Structure, Thermal Analysis and IR Spectroscopic Investigation of $(C_6H_9N_2)H_2XO_4$ (X=As, P). *Mater. Res. Bull.* **2005**, *40*, 2243–2255. doi:10.1016/j.materresbull.2005.06.006.
18. Oueslati, A.; Rayes, A.; Ben Nasr, C.; Lefebvre, F. Synthesis and Characterization of 2-Amino-3-Methylpyridinium Dihy-drogenomonoarsenate. *Mater. Res. Bull.* **2005**, *40*, 1680–1689. doi:10.1016/j.materresbull.2005.05.029.
19. Wilkinson, H.S.; Harrison, W.T.A. Creatininium Dihydrogenarsenate. *Acta Crystallogr., Sect. E* **2005**, *61*, 1228-1230. doi:10.1107/S1600536805016144.
20. Wilkinson, H.S.; Harrison, W.T.A. Guanidinium Dihydrogenarsenate. *Acta Crystallogr., Sect. E* **2005**, *61*, 2023–2025. doi:10.1107/S1600536805028825.
21. Kanagathara, N.; MaryAnjalin, F.; Ragavendran, V.; Dhanasekaran, D.; Usha, R.; Rao, R.G.S.; Marchewka, M.K. Experi-mental and Theoretical (DFT) Investigation of Crystallographic, Spectroscopic and Hirshfeld Surface Analysis of Anilin-ium Arsenate. *J. Mol. Struct.* **2021**, *1223*, 128965. doi:10.1016/j.molstruc.2020.128965.
22. Anbalagan, G.; Marchewka, M.K.; Pawlus, K.; Kanagathara, N. Crystal Structure and Vibrational Spectra of Melaminium Arsenate. *J. Mol. Struct.* **2015**, *1079*, 407–413. doi:10.1016/j.molstruc.2014.09.006.
23. Roshini, S.R.A.; Kanagathara, N.; Marchewka, M.K.; Janczak, J.; Jayalakshmi, D. Growth, Structural, Optical, Morpholog-ical, Thermal, Laser Damage Threshold and Hardness Properties of Organic-Inorganic Crystal: L-Argininium (Bis)Dihydrogenarsenate. *J. Mol. Struct.* **2026**, *1352*, 144499. doi:10.1016/j.molstruc.2025.144499.
24. Beccaria, R.; Pizzi, A.; Chakalov, E.; Resnati, G.; Tolstoy, P. Proton Delocalization in Short Hydrogen Bonds Assembling $HSeO_4^-$ Anions into Supramolecular Adducts. *Phys. Chem. Chem. Phys.* **2025**, *27*, 13601–13617. doi:10.1039/D5CP01211B.

 doi:10.20944/preprints202601.2284.v1

25. Shikina, N. D.; Zotov, A. B.; Tagirov, B. R. Influence of Pressure in the 0.1–100 MPa Interval on the First Dissociation Constant of Arsenous Acid in Water Solutions at 298.15 K. *Russ. J. Phys. Chem. A* **2010**, *84*, 1076–1078. https://doi.org/10.1134/S0036024410060336.
26. CrysAlisPro 1.171.43.136a. Rigaku Oxford Diffraction **2024**.
27. Sheldrick, G. M. SHELXT - Integrated Space-Group and Crystal-Structure Determination. *Acta Crystallogr. A Found. Adv.* **2015**, *71*, 3–8. https://doi.org/10.1107/S2053273314026370.
28. Sheldrick, G. M. Crystal Structure Refinement with SHELXL. *Acta Crystallogr. C Struct. Chem.* **2015**, *71*, 3–8. https://doi.org/10.1107/S2053229614024218.
29. Dolomanov, O. V.; Bourhis, L. J.; Gildea, R. J.; Howard, J. A. K.; Puschmann, H. OLEX2: A Complete Structure Solution, Refinement and Analysis Program. *J. Appl. Crystallogr.* **2009**, *42*, 339–341. https://doi.org/10.1107/S0021889808042726.
30. MacRae, C. F.; Sovago, I.; Cottrell, S. J.; Galek, P. T. A.; McCabe, P.; Pidcock, E.; Platings, M.; Shields, G. P.; Stevens, J. S.; Towler, M.; Wood, P. A. Mercury 4.0: From Visualization to Analysis, Design and Prediction. *J. Appl. Crystallogr.* **2020**, *53*, 226–235. https://doi.org/10.1107/S1600576719014092.
31. Spek, A. L. Structure Validation in Chemical Crystallography. *Acta Crystallogr. D Biol. Crystallogr.* **2009**, *65*, 148–155. https://doi.org/10.1107/S090744490804362X.
32. Dovesi, R.; Erba, A.; Orlando, R.; Zicovich-Wilson, C. M.; Civalleri, B.; Maschio, L.; Rérat, M.; Casassa, S.; Baima, J.; Salustro, S.; Kirtman, B. Quantum-Mechanical Condensed Matter Simulations with CRYSTAL. *Wiley Interdiscip. Rev. Comput. Mol. Sci.* **2018**, *8*, 1–36. https://doi.org/10.1002/wcms.1360.
33. Becke, A. D. A New Mixing of Hartree-Fock and Local Density-Functional Theories. *J. Chem. Phys.* **1993**, *98*, 1372–1377. https://doi.org/10.1063/1.464304.
34. Becke, A. D. Density-Functional Thermochemistry. III. The Role of Exact Exchange. *J. Chem. Phys.* **1993**, *98*, 5648–5652. https://doi.org/10.1063/1.464913.
35. Vilela Oliveira, D.; Laun, J.; Peintinger, M. F.; Bredow, T. BSSE-Correction Scheme for Consistent Gaussian Basis Sets of Double- and Triple-Zeta Valence with Polarization Quality for Solid-State Calculations. *J. Comput. Chem.* **2019**, *40*, 2364–2376. https://doi.org/10.1002/jcc.26013.
36. CRYSTAL - Basis Sets Library. https://www.crystal.unito.it/basis_sets.html.
37. Grimme, S. Semiempirical GGA-Type Density Functional Constructed with a Long-Range Dispersion Correction. *J. Comput. Chem.* **2006**, *27*, 1787–1799. https://doi.org/10.1002/jcc.20495.
38. Civalleri, B.; Zicovich-Wilson, C. M.; Valenzano, L.; Ugliengo, P. B3LYP Augmented with an Empirical Dispersion Term (B3LYP-D*) as Applied to Molecular Crystals. *CrystEngComm* **2008**, *10*, 405–410. https://doi.org/10.1039/b715018k.
39. Dovesi, R.; Saunders, V. R.; Roetti, C.; Orlando, R.; Zicovich-Wilson, C. M.; Pascale, F.; Civalleri, B.; Doll, K.; Harrison, N. M.; Bush, I. J.; D'Arco, P.; Llunell, M.; Causà, M.; Noël, Y.; Maschio, L.; Erba, A.; Rerat, M.; Casassa, S. CRYSTAL17 User's Manual, University of Torino, Torino, 2017; **2018**.
40. Ewald, P. P. Die Berechnung Optischer Und Elektrostatischer Gitterpotentiale. *Ann. Phys.* **1921**, *369*, 253–287. https://doi.org/10.1002/andp.19213690304.
41. Dovesi, R.; Pisani, C.; Roetti, C. Treatment of Coulomb Interactions in Hartree-Fock Calculations of Periodic Systems. *Phys. Rev. B Condens. Matter Mater. Phys.* **1983**, *28*, 5781–5792. https://doi.org/10.1103/PhysRevB.28.5781.
42. Towler, M. D.; Zupan, A.; Causà, M. Density Functional Theory in Periodic Systems Using Local Gaussian Basis Sets. *Comput. Phys. Commun.* **1996**, *98*, 181–205. https://doi.org/10.1016/0010-4655(96)00078-1.
43. Monkhorst, H. J.; Pack, J. D. Special Points for Brillouin-Zone Integrations. *Phys. Rev. B* **1976**, *13*, 5188–5192. https://doi.org/10.1103/PhysRevB.13.5188.
44. Maschio, L. Direct Inversion of the Iterative Subspace (DIIS) Convergence Accelerator for Crystalline Solids Employing Gaussian Basis Sets. *Theor. Chem. Acc.* **2018**, *137*, 1–5. https://doi.org/10.1007/s00214-018-2238-8.
45. Doll, K.; Saunders, V. R.; Harrison, N. M. Analytical Hartree–Fock Gradients for Periodic Systems. *Int. J. Quantum Chem.* **2001**, *82*, 1–13. https://doi.org/10.1002/1097-461X(2001)82:1<1::AID-QUA1017>3.0.CO;2-W.
46. Schlegel, H. B. Geometry Optimization. *Wiley Interdiscip. Rev. Comput. Mol. Sci.* **2011**, *1*, 790–809. https://doi.org/10.1002/wcms.34.

 doi:10.20944/preprints202601.2284.v1

47. Bader, R. F. W. Atoms in Molecules - A Quantum Theory, Vol. 22 of International Series of Monographs in Chemistry, Oxford, UK; Oxford University Press, **1990**.
48. Bertini, L.; Cargnoni, F.; Gatti, C. Chemical Insight into Electron Density and Wave Functions: Software Developments and Applications to Crystals, Molecular Complexes and Materials Science. *Theor. Chem. Acc.* **2007**, *117*, 847–884. https://doi.org/10.1007/s00214-006-0208-z.
49. Gatti, C.; Casassa, S. TOPOND14 User's Manual (CNR-ISTM Milano, Milano, 2014); **2017**.
50. Casassa, S.; Erba, A.; Baima, J.; Orlando, R. Electron Density Analysis of Large (Molecular and Periodic) Systems: A Parallel Implementation. *J. Comput. Chem.* **2015**, *36*, 1940–1946. https://doi.org/10.1002/jcc.24033.
51. Banerjee, A.; Adams, N.; Simons, J. Search for Stationary Points on Surfaces. *J. Phys. Chem.* **1985**, *89*, 52–57. https://doi.org/10.1021/j100247a015.
52. Keith, T. A. PhD Thesis, McMaster University, Hamilton, Ontario, Canada, **1993**.
53. Popelier, P. L. A. A Robust Algorithm to Locate Automatically All Types of Critical Points in the Charge Density and Its Laplacian. *Chem. Phys. Lett.* **1994**, *228*, 160–164. https://doi.org/10.1016/0009-2614(94)00897-3.
54. Frisch, M. J.; Trucks, G. W.; Schlegel, H. B.; Scuseria, G. E.; Robb, M. A.; Cheeseman, J. R.; Scalmani, G.; Barone, V.; Petersson, G. A.; Nakatsuji, H.; Li, X.; Caricato, M.; Marenich, A. V.; Bloino, J.; Janesko, B. G.; Gomperts, R.; Mennucci, B.; Hratchian, H. P.; Ortiz, J. V.; Izmaylov, A. F.; Sonnenberg, J. L.; Williams-Young, D.; Ding, F.; Lipparini, F.; Egidi, F.; Goings, J.; Peng, B.; Petrone, A.; Henderson, T.; Ranasinghe, D.; Zakrzewski, V. G.; Gao, J.; Rega, N.; Zheng, G.; Liang, W.; Hada, M.; Ehara, M.; Toyota, K.; Fukuda, R.; Hasegawa, J.; Ishida, M.; Nakajima, T.; Honda, Y.; Kitao, O.; Nakai, H.; Vreven, T.; Throssell, K.; Montgomery, J. A., Jr. Peralta, J. E.; Ogliaro, F.; Bearpark, M. J.; Heyd, J. J.; Brothers, E. N.; Kudin, K. N.; Staroverov, V. N.; Keith, T. A.; Kobayashi, R.; Normand, J.; Raghavachari, K.; Rendell, A. P.; Burant, J. C.; Iyengar, S. S.; Tomasi, J.; Cossi, M.; Millam, J. M.; Klene, M.; Adamo, C.; Cammi, R.; Ochterski, J. W.; Martin, R. L.; Morokuma, K.; Farkas, O.; Foresman, J. B.; Fox, D. J. Gaussian 16, Revision A.03.
55. Zhao, Y.; Truhlar, D. G. Design of Density Functionals That Are Broadly Accurate for Thermochemistry, Thermochemical Kinetics, and Nonbonded Interactions. *J. Phys. Chem. A* **2005**, *109*, 5656–5667. https://doi.org/10.1021/jp050536c.
56. Rappoport, D.; Furche, F. Property-Optimized Gaussian Basis Sets for Molecular Response Calculations. *J. Chem. Phys.* **2010**, *133*, 134105. https://doi.org/10.1063/1.3484283.
57. Pritchard, B. P.; Altarawy, D.; Didier, B.; Gibson, T. D.; Windus, T. L. New Basis Set Exchange: An Open, Up-to-Date Resource for the Molecular Sciences Community. *J. Chem. Inf. Model.* **2019**, *59*, 4814–4820. https://doi.org/10.1021/acs.jcim.9b00725.
58. Grimme, S.; Ehrlich, S.; Goerigk, L. Effect of the Damping Function in Dispersion Corrected Density Functional Theory. *J. Comput. Chem.* **2011**, *32*, 1456–1465. https://doi.org/10.1002/jcc.21759.
59. Boys, S. F.; Bernardi, F. The Calculation of Small Molecular Interactions by the Differences of Separate Total Energies. Some Procedures with Reduced Errors. *Mol. Phys.* **1970**, *19*, 553–566. https://doi.org/10.1080/00268977000101561.
60. Murray, J. S.; Politzer, P. The Electrostatic Potential: An Overview. *Wiley Interdiscip. Rev. Comput. Mol. Sci.* **2011**, *1*, 153–163. https://doi.org/10.1002/wcms.19.
61. Becke, A. D.; Edgecombe, K. E. A Simple Measure of Electron Localization in Atomic and Molecular Systems. *J. Chem. Phys.* **1990**, *92*, 5397–5403. https://doi.org/10.1063/1.458517.
62. Lu, T.; Chen, F. Multiwfn: A Multifunctional Wavefunction Analyzer. *J. Comput. Chem.* **2012**, *33*, 580–592. https://doi.org/10.1002/jcc.22885.
63. Zhang, J.; Lu, T. Efficient Evaluation of Electrostatic Potential with Computerized Optimized Code. *Phys. Chem. Chem. Phys.* **2021**, *23*, 20323–20328. https://doi.org/10.1039/d1cp02805g.
64. Materials Studio 2017 (17.1.0.48). BIOVIA, Dassault Systèmes. San Diego, CA, USA.
65. Dennington II, R. D.; Keith, T. A.; Millam, J. M. GaussView 6.0.16. Semichem Inc., Shawnee Mission, KS **2016**.
66. Origin 2018. OriginLab. Northampton, MA, USA.

 doi:10.20944/preprints202601.2284.v1

67. Bouaziz, E; Hassen, C. B.; Chniba-Boudjada, N.; Daouda, A.; Mhiri T.; Boujelbene M. Crystal structure, Hirshfeld surface analysis, vibrational, thermal behavior and UV spectroscopy of (2,6-diaminopyridinium) dihydrogen arsenate. *J. Mol. Struct.* **2017**, *1145*, 121e131. Doi: 10.1016/j.molstruc.2017.05.043
68. White, N. G. Antielectrostatically Hydrogen Bonded Anion Dimers: Counter-Intuitive, Common and Consistent. *CrystEngComm* **2019**, *21*, 4855–4858. https://doi.org/10.1039/c9ce01118h.
69. Bader, R. F. W.; Essén, H. The Characterization of Atomic Interactions. *J. Chem. Phys.* **1983**, *80*, 1943–1960. https://doi.org/10.1063/1.446956.
70. Cremer, D.; Kraka, E. A Description of the Chemical Bond in Terms of Local Properties of Electron Density and Energy. *Croat. Chem. Acta* **1984**, *57*, 1259–1281.
71. Koch, U.; Popelier, P. L. A. Characterization of C-H-O Hydrogen Bonds on the Basis of the Charge Density. *J. Phys. Chem.* **1995**, *99*, 9747–9754. https://doi.org/10.1021/j100024a016.
72. Espinosa, E.; Molins, E.; Lecomte, C. Hydrogen Bond Strengths Revealed by Topological Analyses of Experimentally Observed Electron Densities. *Chem. Phys. Lett.* **1998**, *285*, 170–173. https://doi.org/10.1016/S0009-2614(98)00036-0.
73. Jenkins, S.; Morrison, I. The Chemical Character of the Intermolecular Bonds of Seven Phases of Ice as Revealed by Ab Initio Calculation of Electron Densities. *Chem. Phys. Lett.* **2000**, *317*, 97–102. https://doi.org/10.1016/S0009-2614(99)01306-8.
74. Gatti, C.; May, E.; Destro, R.; Cargnoni, F. Fundamental Properties and Nature of CH··O Interactions in Crystals on the Basis of Experimental and Theoretical Charge Densities. The Case of 3,4-Bis(Dimethylamino)-3-Cyclobutene-1,2-Dione (DMACB) Crystal. *J. Phys. Chem. A* **2002**, *106*, 2707–2720. https://doi.org/10.1021/jp013980y.
75. Gatti, C. Chemical Bonding in Crystals: New Directions. *Z. Krist.* **2005**, *220*, 399–457. https://doi.org/10.1524/zkri.220.5.399.65073.
76. Grabowski, S. J. What Is the Covalency of Hydrogen Bonding? *Chem. Rev.* **2011**, *111*, 2597–2625. https://doi.org/10.1021/cr800346f.
77. Espinosa, E.; Alkorta, I.; Elguero, J.; Molins, E. From Weak to Strong Interactions: A Comprehensive Analysis of the Topological and Energetic Properties of the Electron Density Distribution Involving X-H···F-Y Systems. *J. Chem. Phys.* **2002**, *117*, 5529–5542. https://doi.org/10.1063/1.1501133.
78. Vener, M. V.; Manaev, A. V.; Egorova, A. N.; Tsirelson, V. G. QTAIM Study of Strong H-Bonds with the O–H···A Fragment (A = O, N) in Three-Dimensional Periodical Crystals. *J. Phys. Chem. A* **2007**, *111*, 1155–1162. https://doi.org/10.1021/jp067057d.
79. Mata, I.; Alkorta, I.; Espinosa, E.; Molins, E. Relationships between Interaction Energy, Intermolecular Distance and Electron Density Properties in Hydrogen Bonded Complexes under External Electric Fields. *Chem. Phys. Lett.* **2011**, *507*, 185–189. https://doi.org/10.1016/j.cplett.2011.03.055.
80. Vener, M. V.; Egorova, A. N.; Churakov, A. V.; Tsirelson, V. G. Intermolecular Hydrogen Bond Energies in Crystals Evaluated Using Electron Density Properties: DFT Computations with Periodic Boundary Conditions. *J. Comput. Chem.* **2012**, *33*, 2303–2309. https://doi.org/10.1002/jcc.23062.
81. Bandura, A. V.; Kubicki, J. D.; Sofo, J. O. Comparisons of Multilayer H_2O Adsorption onto the (110) Surfaces of α-TiO_2 and SnO_2 as Calculated with Density Functional Theory. *J. Phys. Chem. B* **2008**, *112*, 11616–11624. https://doi.org/10.1021/jp711763y.
82. Evarestov, R. A.; Bandura, A. V.; Losev, M. V.; Piskunov, S.; Zhukovskii, Y. F. Titania Nanotubes Modeled from 3- and 6-Layered (1 0 1) Anatase Sheets: Line Group Symmetry and Comparative Ab Initio LCAO Calculations. *Physica E Low Dimens. Syst. Nanostruct.* **2010**, *43*, 266–278. https://doi.org/10.1016/j.physe.2010.07.068.
83. Laskowski, R.; Blaha, P. Understanding of ^{33}S NMR Shielding in Inorganic Sulfides and Sulfates. *J. Phys. Chem. C* **2015**, *119*, 731–740. https://doi.org/10.1021/jp5095933.
84. Treviño, P.; Garcia-Castro, A. C.; López-Moreno, S.; Bautista-Hernández, A.; Bobocioiu, E.; Reynard, B.; Caracas, R.; Romero, A. H. Anharmonic Contribution to the Stabilization of $Mg(OH)_2$ from First Principles. *Phys. Chem. Chem. Phys.* **2018**, *20*, 17799–17808. https://doi.org/10.1039/C8CP02490A.
85. Evarestov, R. A.; Kuzmin, A. Topological Analysis of Chemical Bonding in the Layered $FePSe_3$ upon Pressure-Induced Phase Transitions. *J. Comput. Chem.* **2020**, *41*, 2610–2623. https://doi.org/10.1002/jcc.26416.

 doi:10.20944/preprints202601.2284.v1

86. Dronskowski, R.; Peter, E. B. Crystal Orbital Hamilton Populations (COHP). Energy-Resolved Visualization of Chemical Bonding in Solids Based on Density-Functional Calculations. *J. Phys. Chem.* **1993**, *97*, 8617–8624. https://doi.org/10.1021/j100135a014.
87. Deringer, V. L.; Tchougréeff, A. L.; Dronskowski, R. Crystal Orbital Hamilton Population (COHP) Analysis As Projected from Plane-Wave Basis Sets. *J. Phys. Chem. A* **2011**, *115*, 5461–5466. https://doi.org/10.1021/jp202489s.
88. Maintz, S.; Deringer, V. L.; Tchougréeff, A. L.; Dronskowski, R. Analytic Projection from Plane-Wave and PAW Wavefunctions and Application to Chemical-Bonding Analysis in Solids. *J. Comput. Chem.* **2013**, *34*, 2557–2567. https://doi.org/10.1002/jcc.23424.
89. Ruggiero, M. T.; Erba, A.; Korter, T. M. Origins of Contrasting Copper Coordination Geometries in Crystalline Copper Sulfate Pentahydrate. *Phys. Chem. Chem. Phys.* **2015**, *17*, 31023–31029. https://doi.org/10.1039/C5CP05554G.
90. Deringer, V. L.; Englert, U.; Dronskowski, R. Covalency of Hydrogen Bonds in Solids Revisited. *Chem. Commun.* **2014**, *50*, 11547–11549. https://doi.org/10.1039/C4CC04716H.
91. Deringer, V. L.; George, J.; Dronskowski, R.; Englert, U. Plane-Wave Density Functional Theory Meets Molecular Crystals: Thermal Ellipsoids and Intermolecular Interactions. *Acc. Chem. Res.* **2017**, 50, 1231–1239. https://doi.org/10.1021/acs.accounts.7b00067.